

Full Surround Monodepth from Multiple Cameras

Vitor Guizilini^{1*} Igor Vasiljevic^{2*} Rareş Ambruş¹ Greg Shakhnarovich² Adrien Gaidon¹

¹Toyota Research Institute
{first.lastname}@tri.global

²Toyota Technological Institute at Chicago
{ivas, greg}@ttic.edu

Abstract

Self-supervised monocular depth and ego-motion estimation is a promising approach to replace or supplement expensive depth sensors such as LiDAR for robotics applications like autonomous driving. However, most research in this area focuses on a single monocular camera or stereo pairs that cover only a fraction of the scene around the vehicle. In this work, we extend monocular self-supervised depth and ego-motion estimation to large-baseline multi-camera rigs. Using generalized spatio-temporal contexts, pose consistency constraints, and carefully designed photometric loss masking, we learn a single network generating dense, consistent, and scale-aware point clouds that cover the same full surround 360° field of view as a typical LiDAR scanner. We also propose a new scale-consistent evaluation metric more suitable to multi-camera settings. Experiments on two challenging benchmarks illustrate the benefits of our approach over strong baselines.

1. Introduction

Self-supervised learning is a promising tool for 3D perception in robotics, forming an integral part of modern state-of-the-art depth estimation architectures [12, 14, 15, 55]. With the potential to complement or even replace expensive LiDAR sensors, these methods typically take as input a monocular stream of images and produce dense depth and ego-motion predictions. Though recently released datasets contain multi-camera data that cover the same full 360° field of view as LiDAR [5, 15], research has focused on forward-facing cameras or stereo pairs. In this paper, we extend self-supervised depth and ego-motion learning to the general multi-camera setting, where cameras can have different intrinsics and minimally overlapping regions, as required to minimize the number of cameras on the platform while providing full 360° coverage. We describe why stereo-based learning techniques do not apply in this setting, and show that batching cameras independently does not effectively leverage all information available in a multi-camera dataset.

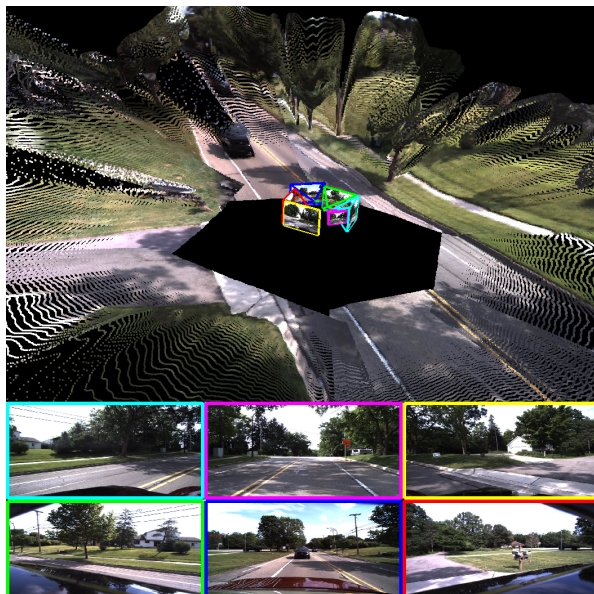


Figure 1: Consistent scale-aware Full Surround Monodepth (FSM) pointcloud from multiple cameras.

We propose instead to leverage *cross-camera temporal contexts* via *spatio-temporal photometric constraints* to increase the amount of overlap between cameras thanks to the system’s ego-motion. By exploiting known extrinsics between cameras, and enforcing *pose consistency constraints* to ensure all cameras follow the same rigid body motion, we are able to learn *scale-aware models* without any ground-truth depth or ego-motion labels. Furthermore, our multi-camera constraints enable the prediction of consistent 360° point clouds, as reflected in our proposed *shared median-scaling* evaluation protocol. Finally, we find that *masking out non-overlapping and self-occluded areas* during photometric loss calculation has a drastic impact on performance.

In summary, our contributions are as follows:

- We demonstrate, for the first time, self-supervised learning of scale-aware and consistent depth networks in a wide-baseline 360° multi-camera setting, which we refer to as **Full Surround Monodepth (FSM)**.

- We introduce key techniques to extend self-supervised depth and ego-motion learning to wide-baseline multi-camera systems: **multi-camera spatio-temporal contexts** and **pose consistency constraints**, as well as study the **impact of non-overlapping and self-occlusion photometric masking** in this novel setting.
- We ablate and show the benefits of our proposed approach on **two publicly available multi-camera datasets**: *DDAD* [15] and *nuScenes* [5].

2. Related Work

Learning with Stereo Supervision. Depth estimation from a rectified stereo pair is a classical task in computer vision [4, 39]. In this setting, the 2D matching problem is greatly simplified to a 1D disparity search. In recent years, supervised stereo depth estimation methods [26, 52, 53], as well as self-supervised techniques [9, 11, 31], have emerged as competitive learning-based approaches to this task. Self-supervised methods take advantage of rectified stereo training data with large overlap to train a disparity estimation network. Our proposed method is intended for multi-camera configurations with very large baselines (and thus minimal image overlap) where stereo rectification, and by extension disparity estimation, is not feasible.

Monocular Depth Estimation. Early approaches to learning-based depth estimation were fully supervised [7, 8, 40], using datasets collected using IR [36] or laser scanners [10]. Although achieving impressive results compared to non-learning baselines, these methods suffered from sparsity and high noise levels in the “ground-truth” data, as well as the need for additional sensors during data collection. The pioneering work of Zhou *et al.* [55] introduced the concept of self-supervised learning of depth and ego-motion by casting this problem as a task of view synthesis, using an image reconstruction objective. Further improvements in the view synthesis loss [12] and network architectures [16], have lead to accuracy that competes with supervised approaches [12, 14, 15, 29]. These learned depth estimators have found applications in several areas, including 3D object detection, where “pseudo-LiDAR” [46] point cloud estimates obtained from monocular depth maps are used to predict 3D bounding boxes. However, these methods are designed for either monocular or rectified stereo images, and thus only capture a narrow slice of the LiDAR point cloud (typically less than 180°). Consistent multi-camera depth estimation would allow these methods to operate on the full 360° point cloud annotations.

Omnidirectional Depth Estimation. A popular approach to 360° depth estimation is through equirectangular or omnidirectional images [1, 2, 6, 23, 42, 44, 45]. These methods operate on panoramic images to estimate depth, either monocular or through stereo [49]. For robotics tasks,

these images suffer from major disadvantages as a 360° representation: (1) annotated datasets generally consist of perspective images, making transfer difficult; (2) specialized architectures are necessary; and (3) network training is limited by GPU memory, so resolution must be sacrificed to train using images with such a large field of view.

Catadioptric cameras are an example of an “omnidirectional” camera, and a self-supervised generalized camera model was proposed [43] that produces 360° point clouds from single images. However, the resolution of catadioptric images drops dramatically at range, while our proposed approach generates much higher resolution pointclouds using perspective cameras.

Deep Multi-view Stereo. Our multi-camera setting is related to the multi-view stereo (MVS) learning literature, which are generally supervised approaches where learned matching allows a network to predict matching cost-volumes [18, 19, 22, 34, 51]. Khot *et al.* [27] relax the supervision requirements and propose a self-supervised MVS architecture, taking insights from self-supervised monocular depth estimation and using a photometric loss. However, their proposed setting assumes a large collection of images surrounding a single object with known relative pose and large overlap for cost volume computation, and is thus very different from our setting – our architecture is designed to work with image sequences from any location and with arbitrarily small overlapping between cameras.

3. Methodology

We first describe the standard approach to single camera monocular self-supervised depth and ego-motion learning. Afterwards, we extend the description to our multi-camera setting and detail our three technical contributions.

3.1. Single-Camera Monodepth

Self-supervised depth and ego-motion architectures consist of a depth network that produces depth maps \hat{D}_t for a target image I_t , as well as a pose network that predicts the relative pose for pairs of target t and context c frames. This pose prediction is a rigid transformation $\hat{\mathbf{X}}^{t \rightarrow c} = \begin{pmatrix} \hat{\mathbf{R}}_0^{t \rightarrow c} & \hat{\mathbf{t}}_1^{t \rightarrow c} \\ \mathbf{0} & \mathbf{1} \end{pmatrix} \in \text{SE}(3)$. We train the networks jointly by minimizing the reprojection error between the actual target image I_t and the synthesized image \hat{I}_t , obtaining the latter by projecting pixels from the context image I_c (usually preceding or following I_t in a sequence) onto the target image I_t [55]. The photometric reprojection loss [11, 55] consists of a structure similarity (SSIM) metric and an L1 loss term [48]:

$$\mathcal{L}_p(I_t, \hat{I}_t) = \alpha \frac{1 - \text{SSIM}(I_t, \hat{I}_t)}{2} + (1 - \alpha) \|I_t - \hat{I}_t\| \quad (1)$$

To synthesize the target image, as in Zhou *et al.* [55], we use STN [21] via grid sampling with bilinear interpolation.

This view synthesis operation is thus fully differentiable, enabling gradient back-propagation for end-to-end training. We define the pixel-warping operation as:

$$\hat{\mathbf{p}}^t = \pi(\hat{\mathbf{R}}^{t \rightarrow c} \phi(\mathbf{p}^t, \hat{d}^t, \mathbf{K}) + \hat{\mathbf{t}}^{t \rightarrow c}, \mathbf{K}) \quad (2)$$

where $\phi(\mathbf{p}, \hat{d}, \mathbf{K}) = \mathbf{P}$ is the unprojection of a pixel in homogeneous coordinates \mathbf{p} to a 3D point \mathbf{P} for a given estimated depth \hat{d} . Denote the projection of a 3D point back onto the image plane as $\pi(\mathbf{P}, \mathbf{K}) = \mathbf{p}$. Both operations require the camera parameters, which for the standard pinhole model [17] is defined by the 3×3 intrinsics matrix \mathbf{K} .

3.2. Multi-Camera Spatio-Temporal Contexts

Multi-camera approaches to self-supervised depth and ego-motion are currently restricted to the stereo setting with rectified images that enable predicting disparities [11], which are then converted to depth through a known baseline. Although methods have been proposed that combine stereo and monocular self-supervision [12, 47], directly regressing depth also from stereo pairs, these still assume the availability of highly-overlapping images, from datasets such as KITTI [10]. Our proposed approach differs from the stereo setting in the sense that it *does not require stereo-rectified or highly-overlapping images*, but rather is capable of exploiting small overlaps (as low as 10%) between cameras with arbitrary locations as a way to both *improve individual camera performance* and generate *scale-aware* models from known extrinsics. Multi-camera rigs with such low overlap are common, e.g., in autonomous driving as a cost-effective solution to 360° vision [5, 15].

Let C_i and C_j be two cameras with extrinsics \mathbf{X}_i and \mathbf{X}_j , and intrinsics \mathbf{K}_i and \mathbf{K}_j . Denoting the relative extrinsics as $\mathbf{X}_{i \rightarrow j}$ and abbreviating $\phi_i(\mathbf{p}, \hat{d}) = \phi(\mathbf{p}, \hat{d}, \mathbf{K}_i)$ and $\pi_i(\mathbf{P}) = \pi(\mathbf{P}, \mathbf{K}_i)$, we can use Equation 2 to warp images from these two cameras:

$$\hat{\mathbf{p}}_i = \pi_j(\mathbf{R}_{i \rightarrow j} \phi_i(\mathbf{p}_i, \hat{d}_i) + \mathbf{t}_{i \rightarrow j}) \quad (3)$$

Note that the above equation is purely *spatial*, since it warps images between different cameras taken at the same timestep. Conversely, Equation 2 is purely *temporal*, since it is only concerned with warping images from the same camera taken at different timesteps.

Therefore, for any given camera C_i at a timestep t , a context image can be either temporal (i.e., from adjacent frames $t - 1$ and $t + 1$) or spatial (i.e., from any camera j that overlaps with i). This allows us to further generalize the concept of “context image” in self-supervised learning to also include temporal contexts from other overlapping cameras. This is done by warping images between different cameras taken at different timesteps using a composition of known extrinsics with predicted ego-motion:

$$\hat{\mathbf{p}}_i^t = \pi_j(\mathbf{R}_{i \rightarrow j}(\hat{\mathbf{R}}_j^{t \rightarrow c} \phi_j(\mathbf{p}_j^t, \hat{d}_j^t) + \hat{\mathbf{t}}_j^{t \rightarrow c}) + \mathbf{t}_{i \rightarrow j}) \quad (4)$$

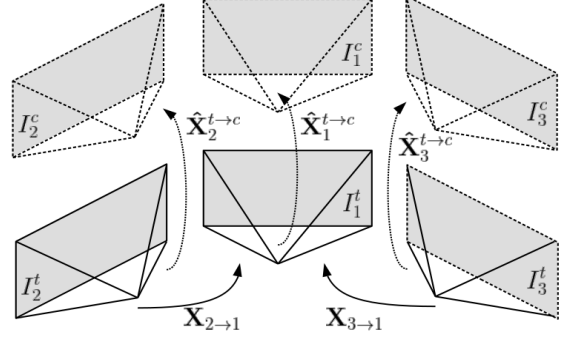


Figure 2: **Multi-camera spatio-temporal transformation matrices.** Solid cameras are *target* (current frames), and dotted cameras are *context* (adjacent frames). Spatial transformations ($\mathbf{X}_{i \rightarrow 1}$) are obtained from known extrinsics, and temporal transformations ($\hat{\mathbf{X}}_i^{t \rightarrow c}$) from the pose network.

A diagram depicting such transformations can be found in Figure 2, and Figure 3 shows examples of warped images and corresponding photometric losses using the DDAD dataset [15]. Particularly, the fifth and sixth rows show examples of multi-camera photometric losses using purely spatial contexts (Equation 3) and our proposed spatio-temporal contexts (Equation 4). As we can see, *spatio-temporal contexts (STC) promote a larger overlap between cameras and smaller residual photometric loss*, due to occlusions and changes in brightness and viewpoint. This improved photometric loss leads to *better self-supervision* for depth and ego-motion learning in a multi-camera setting, as validated in experiments.

3.3. Multi-Camera Pose Consistency Constraints

Beyond cross-camera constraints due to image overlap, there are also natural pose constraints due to the fact that all cameras are rigidly attached to a single vehicle (i.e., relative camera extrinsics are constant and fixed). Specifically, the pose network is used to predict independent poses for each camera, even though they should correspond to the same transformation, just in a different coordinate frame. For a given camera i , the pose network predicts its transformation $\hat{\mathbf{X}}_i^{t \rightarrow t+1}$ from the current frame t to the subsequent frame $t + 1$. In order to obtain predictions from different cameras that are in the same coordinate frame, we transform this prediction to the coordinate frame of a “canonical” camera C_j . We denote $\hat{\mathbf{X}}_i^{t \rightarrow t+1}$ in C_j coordinates as $\tilde{\mathbf{X}}_i^{t \rightarrow t+1}$.

To convert a predicted transformation $\hat{\mathbf{X}}_i^{t \rightarrow t+1}$ from the coordinate frame of camera C_i to camera C_j , we can use the extrinsics \mathbf{X}_i and \mathbf{X}_j to generate $\tilde{\mathbf{X}}_i^{t \rightarrow t+1}$ as follows:

$$\tilde{\mathbf{X}}_i^{t \rightarrow t+1} = \mathbf{X}_j^{-1} \mathbf{X}_i \hat{\mathbf{X}}_i^{t \rightarrow t+1} \mathbf{X}_i^{-1} \mathbf{X}_j \quad (5)$$

where $\tilde{\mathbf{X}}_i^{t \rightarrow t+1} = \begin{pmatrix} \tilde{\mathbf{R}}_i^{t \rightarrow t+1} & \tilde{\mathbf{t}}_i^{t \rightarrow t+1} \\ \mathbf{0} & \mathbf{1} \end{pmatrix}$. As a convention, we convert all predicted transformations to the coordinate

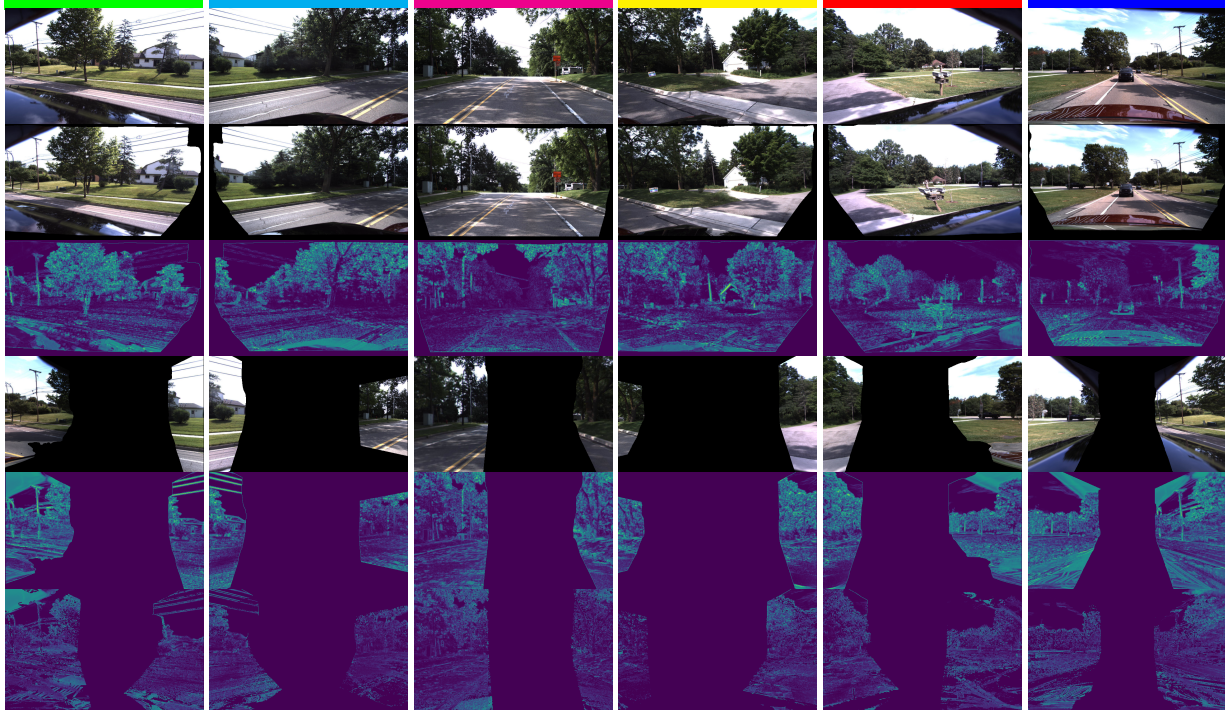


Figure 3: **Examples of spatial and temporal image warping** on the *DDAD* dataset (camera colors from Figure 1, clockwise). **First row:** Input RGB images. **Second and third rows:** Synthesized views from temporal contexts (Equation 2) and photometric losses. **Fourth and fifth rows:** Synthesized views from surrounding cameras (Equation 3), and photometric losses using only spatial contexts. **Sixth row** Photometric losses using our proposed spatio-temporal contexts. By also leveraging temporal contexts during cross-camera photometric warping, we are able to generate larger overlapping areas between images, as well as a smaller residual photometric error (darker colors) for optimization.

frame of the front camera C_1 . Once all predictions are in the same coordinate frame, we constrain the translation vectors \mathbf{t} and rotation matrices \mathbf{R} to be similar across all cameras.

Translation. We constrain all predicted translation vectors to be similar to the prediction for the *front camera*, which generally performs best across all experiments. Defining the predicted front camera translation vector as $\hat{\mathbf{t}}_1^{t+1}$, for N cameras the translation consistency loss is given by:

$$\mathbf{t}_{loss} = \sum_{j=2}^N \|\hat{\mathbf{t}}_1^{t+1} - \tilde{\mathbf{t}}_j^{t+1}\|^2 \quad (6)$$

Rotation. Similarly, we want to constrain other cameras to predict a rotation matrix similar to the front camera. To accomplish that, once the predictions are in the same coordinate frame we convert them to Euler angles $(\phi_i, \theta_i, \psi_i)$ and calculate the rotation consistency loss such that:

$$\mathbf{R}_{loss} = \sum_{j=2}^N \|\hat{\phi}_1 - \tilde{\phi}_j\|^2 + \|\hat{\theta}_1 - \tilde{\theta}_j\|^2 + \|\hat{\psi}_1 - \tilde{\psi}_j\|^2 \quad (7)$$

Similar to the trade-off between rotation losses and translation loss in the original PoseNet [25, 24], we trade off between the two constraints by defining $\mathcal{L}_{pcc} = \alpha_t \mathbf{t}_{loss} + \alpha_r \mathbf{R}_{loss}$, where α_t and α_r are weight coefficients.

3.4. The Importance of Masks

The photometric loss, as used for self-supervised monocular depth and ego-motion learning, has several assumptions that are not entirely justified in real-world scenarios. These include the static world assumption (violated by dynamic objects), brightness constancy (violated by luminosity changes), and dense overlap between frames (violated by large viewpoint changes). Although several works have been proposed to relax some of these assumptions [14], more often than not methods are developed to mask out those regions [12], to avoid spurious information from contaminating the final model.

In a multi-camera setting there are two scenarios that are particularly challenging for self-supervised depth and ego-motion learning: *non-overlapping areas*, due to large changes in viewpoint between cameras, and *self-occlusions*, due to camera positioning that results in the platform (i.e., ego-vehicle) partially covering the image. Here we describe how our proposed approach addresses each of these scenarios. The final masked photometric loss used during training (Equation 1) takes the form:

$$\mathcal{L}_{mp}(I_t, \hat{I}_t) = \mathcal{L}_p(I_t, \hat{I}_t) \odot \mathcal{M}_{no} \odot \mathcal{M}_{so} \quad (8)$$

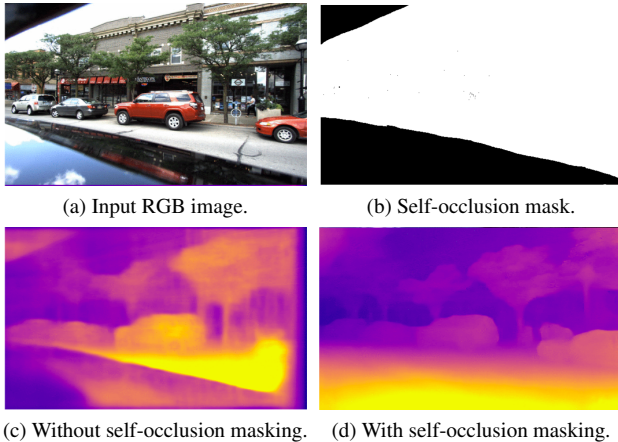


Figure 4: **Impact of self-occlusion masks on depth estimation** on the *DDAD* dataset. These masks remove self-occluded regions from the self-supervised photometric loss, enabling easier optimization (lower loss, cf. Figure 3) and better generalization (e.g., on the ground plane).

where \odot denotes element-wise multiplication, and \mathcal{M}_{no} and \mathcal{M}_{so} are binary masks respectively for non-overlapping and self-occluded areas, as described below.

3.4.1 Non-Overlapping Areas

We generate non-overlapping area masks by jointly warping with each context image a unitary tensor of the same spatial dimensions, using nearest-neighbor interpolation. The warped tensor is used to mask the photometric loss, thus avoiding gradient backpropagation in areas where there is no overlap between frames. Note that this unitary warping also uses network predictions, and therefore is constantly updated at training time. This is similar to the motion masks described in [35], however here we extend this concept to a spatio-temporal multi-camera setting. Figure 3 shows examples of spatial and temporal non-overlapping masks on the *DDAD* dataset, with a trained model. As expected, temporal contexts have a large amount of frame-to-frame overlap ($> 90\%$), even considering side-pointing cameras. Spatial context overlaps, on the other hand, are much smaller ($10 - 20\%$), due to radically different camera orientations.

3.4.2 Self-Occlusions

A common technique in self-supervised learning is the “auto-mask” procedure, which filters out pixels with a synthesized reprojection error higher than the original source image [12]. This mask particularly targets the “infinite depth problem”, which occurs when scene elements move at the same speed as the vehicle, causing zero parallax and thus an infinitely-far away depth estimate for that region.

However, this technique assumes brightness constancy, and the self-occlusions created by the robot (or car) body are often highly specular (Figure 4a), especially in the case of modern passenger vehicles.

Using a network with auto-masking enabled, specular self-occlusions create serious errors in the depth predictions, as shown in Figure 4c. We propose a simpler approach, consisting of creating manual masks for each camera (this needs only to be done once, assuming that the extrinsics remain constant). As shown in Figure 4d, and ablated in experiments, the introduction of these self-occlusion masks results in a substantial improvement in overall performance, to the point of enabling self-supervised depth and ego-motion learning under these conditions. Interestingly, self-occluded areas in the predicted depth maps are correctly “inpainted” to include the hidden ground plane. We posit that this is due to multi-camera training, in which a region unoccluded in one camera can be used to resolve self-occlusions in another camera.

4. Experiments

4.1. Datasets

Traditionally, self-supervised depth and ego-motion learning uses monocular sequences [55, 12, 14, 15] or rectified stereo pairs [12, 38] from forward-facing cameras in the KITTI [10] dataset. Recently, several datasets have been released with synchronized multi-camera sequences that cover the entire surrounding of the ego-vehicle [5, 15]. We focus on these datasets for our experiments, showing that our proposed approach, FSM, produces substantial improvements across all cameras. For more information on these datasets, please refer to the supplementary material.

KITTI [10]. The KITTI dataset is the standard benchmark for depth and ego-motion estimation. Although it only contains forward-facing stereo pairs, we show that FSM accommodates the special case of high-overlapping rectified images, achieving competitive results with stereo methods.

DDAD [15]. The DDAD dataset is the main focus of our experiments, since it contains six cameras with relatively small overlap and highly accurate dense ground-truth depth maps for evaluation. We show that, by jointly training FSM on all cameras, we considerably improve results and establish a new state of the art on this dataset by a large margin.

NuScenes [5]. The nuScenes dataset is a popular benchmark for 2D and 3D object detection, as well as semantic and instance segmentation. However, it is a challenging dataset for self-supervised depth estimation because of the relatively low resolution of the images, very small overlap between the cameras, high diversity of weather conditions and time of day, and unstructured environments. We show that FSM is robust enough to overcome these challenges and substantially improve results relative to the baseline.



(a) Monocular photometric loss (Abs Rel 0.211/0.241)



(b) Spatio-temporal photometric loss (Abs Rel 0.201/0.207)

Figure 5: **Multi-camera pointcloud alignment** on DDAD using (a) the standard monocular photometric loss, and (b) our proposed spatio-temporal photometric constraints. We also report per-frame and shared median-scaling Abs Rel results (average of all cameras, see Table 3 for more details).

4.2. Multi-Camera Depth Evaluation Metrics

Our approach is *scale-aware*, due to its use of known extrinsics to generate metrically accurate predictions. In contrast, existing self-supervised monocular depth and ego-motion architectures learn up-to-scale models, resorting to *median-scaling* at test time in order to compare depth predictions against the (scaled) ground truth. Median scaling “borrows” the true scale of ground truth by multiplying each depth estimate by $\frac{\text{med}(D_{gt})}{\text{med}(D_{pred})}$, where *med* is the median operation and D_{gt} and D_{pred} are ground-truth and predicted depth maps. This scaling enables quantitative evaluation, but requires ground truth information at test time, limiting the utility of such methods in real-world applications.

Furthermore, median-scaling hides certain undesired behaviors, such as frame-to-frame variability [3]. This is exacerbated in the setting proposed in this paper, where multiple images are used to generate a single, consistent pointcloud. If median-scaling is applied on a per-frame basis, the resulting depth maps will hide any scale discrepancies between camera predictions, which will not be reflected in the quantitative evaluation (Figure 5). Thus, instead of the standard median-scaling protocol, we propose to use a single scale factor γ shared by all N considered cameras defined as:

$$\gamma = \frac{\text{med}(\{D_{gt}^1, \dots, D_{gt}^N\})}{\text{med}(\{D_{pred}^1, \dots, D_{pred}^N\})} \quad (9)$$

This is similar to single median-scaling [12], in which the same factor is used to scale predictions for the entire *dataset*. In our setting, because multiple images are considered jointly, we instead produce a shared factor to scale all predictions at that *timestep*. This forces all predicted depth maps in the same timestep to have the same scale factor

(and thus be relatively consistent), with any deviation reflected in the calculated metrics. In practice, as our method is scale-aware, we report metrics both with (for comparison with baselines) and without median-scaling.

4.3. Networks

For all of our experiments, we used a ResNet18-based depth and pose networks, based on *monodepth2* [12]. For more details regarding network architectures and training schedules, please refer to our supplementary material.

4.4. Stereo Methods

Though our proposed approach is intended for multi-camera rigs with small overlap, it can also be used without modification on stereo datasets, allowing us to learn depth directly without rectifying the images for disparity learning. We show in Table 1 that despite the greater simplicity of stereo rectification on the KITTI dataset, our approach remains competitive with explicitly stereo methods.

4.5. Single-Camera Methods

Given that the majority of self-supervised monocular depth estimation papers focuses on single-image sequences with forward-facing cameras, we consider a variety of alternative baselines for our quantitative evaluation. In particular, we pick two state-of-the-art published methods: *monodepth2* [12], that uses a simpler architecture with a series of modifications to the photometric loss calculation; and *PackNet* [15], that proposes an architecture especially designed for self-supervised depth learning. We use results of these methods for the front camera, as reported by Guizilini *et al.* [15], as baselines for our method.

We also take inspiration from the “Learning SfM from SfM” work [30, 33] and employ COLMAP [41], a state-of-the-art structure-from-motion system, on the unlabeled DDAD [15] training split to generate predicted depth maps, that are then used as pseudo-labels for supervised learning. Note that, while this approach is also self-supervised (i.e., there is no ground-truth depth), it requires substantially more computation, since it processes all images from

Method	Sup.	Abs Rel↓	Sq Rel↓	RMSE↓	$\delta_{1.25}$ ↑
UnDeepVO [32]	<i>S</i>	0.183	1.730	6.570	-
Godard et al. [11]	<i>S</i>	0.148	1.344	5.927	0.803
SuperDepth [38]	<i>S</i>	0.112	0.875	4.958	0.852
Monodepth2 [12]	<i>M</i>	0.115	0.903	4.863	0.877
Monodepth2 [12]	<i>S</i>	0.109	0.873	4.960	0.864
Monodepth2 [12]	<i>M + S</i>	0.106	<u>0.818</u>	<u>4.750</u>	0.874
FSM	<i>M + S</i>	<u>0.108</u>	0.737	4.615	<u>0.872</u>

Table 1: **Depth estimation results on the KITTI dataset**, relative to stereo methods. Even though our approach relaxes several stereo assumptions, it remains competitive with published methods.

Method	Abs Rel \downarrow	Sq Rel \downarrow	RMSE \downarrow	$\delta_{1.25}\uparrow$
COLMAP (pseudo-depth)	0.243	4.438	17.239	0.601
Monodepth2 (R18) [12]	0.213	4.975	18.051	0.761
Monodepth2 (R50) [12]	0.198	4.504	16.641	0.781
PackNet [15]	0.162	3.917	13.452	0.823
FSM (w/o mask & spatial)	0.184	4.049	17.109	0.735
FSM (w/o spatial)	0.139	3.023	14.106	0.827
FSM* (w/ spatial)	0.135	2.841	13.850	0.832
FSM* (w/ spatio-temporal)	0.130	2.731	13.654	0.837

Table 2: **Quantitative depth evaluation of different methods on the DDAD [15] dataset**, for distances up to 200m on the forward-facing camera. The symbol * indicates a *scale-aware* model, evaluated without median-scaling at test time.

any given sequence simultaneously with a series of bundle adjustment techniques to produce a single reconstruction of the entire scene. For more details regarding this baseline, please refer to the supplementary material.

The results of these experiments are summarized in Table 2. Compared to other self-supervised methods on monocular sequences, our masking procedures for multi-camera training already significantly improve results from the previous state of the art [15]: from 0.162 to 0.139 absolute relative error (Abs Rel) on the front camera. By introducing spatial contexts (Equation 3), we not only further improve performance, but also learn *scale-aware* models by leveraging the camera extrinsics. Note that there is no limitation on the extrinsics transformation, only the assumption of some overlap between camera pairs (Figure 3). Finally, by introducing our proposed spatio-temporal contexts (Equation 4) and pose consistency constraints (Section 3.3) we further boost performance to 0.130, thus **achieving a new state of the art by a large margin**.

4.6. Multi-Camera Depth Estimation

We now evaluate FSM depth performance on all cameras of the *DDAD* and *nuScenes* datasets, ablating the impact of our contributions in the multi-camera setting (see Table 3).

4.6.1 Photometric Masking

As a baseline, we combine images from all cameras into a single dataset, without considering masking or cross-camera constraints. This is similar to Gordon *et al.* [14], where multiple datasets from different cameras are pooled together to train a single model. As discussed in Section 3.4.2, the presence of self-occlusions on the *DDAD* dataset severely degrades depth performance when masking is not considered, reaching 0.380 Abs Rel (average of all cameras) versus 0.211 when self-occlusion masks are introduced (see Figure 4 for a qualitative comparison). Note that these results are still unscaled, and therefore median-scaling is required at test time for a proper quantitative evaluation.

Method	Abs.Rel. \downarrow						
	Front	F.Left	F.Right	B.Left	B.Right	Back	Avg.
Mono † - M	0.184	0.366	0.448	0.417	0.426	0.438	0.380
Mono †	0.139	0.209	0.236	0.231	0.247	0.204	0.211
FSM†	<u>0.131</u>	<u>0.203</u>	<u>0.226</u>	0.223	0.240	0.188	<u>0.202</u>
Mono ‡	0.143	0.238	0.265	0.277	0.276	0.247	0.241
FSM‡	0.133	0.212	0.229	0.231	<u>0.246</u>	0.194	0.208
FSM - STC	0.133	0.219	0.246	0.252	0.259	0.197	0.218
FSM - PCC	<u>0.131</u>	0.206	0.228	0.238	0.248	<u>0.188</u>	0.207
FSM	0.130	0.201	0.224	<u>0.229</u>	0.240	0.186	0.201

(a) DDAD

Method	Abs.Rel. \downarrow						
	Front	F.Left	F.Right	B.Left	B.Right	Back	Avg.
Mono †	0.214	0.304	0.388	0.314	0.438	0.304	0.327
FSM†	0.198	0.297	0.364	<u>0.301</u>	0.392	<u>0.240</u>	<u>0.299</u>
Mono ‡	0.251	0.403	0.546	0.429	0.616	0.321	0.428
FSM‡	0.200	0.337	0.448	0.354	0.521	0.267	0.355
FSM - STC	0.208	0.382	0.510	0.393	0.595	0.258	0.391
FSM - PCC	<u>0.187</u>	<u>0.291</u>	0.392	0.311	0.448	0.235	0.311
FSM	0.186	0.287	<u>0.375</u>	0.296	<u>0.418</u>	0.221	0.297

(b) nuScenes

Table 3: **Depth estimation results on multi-camera datasets**, using *FSM* relative to the single-camera photometric loss (*Mono*). The symbol † denotes per-frame median-scaling, and ‡ shared median-scaling (Eq. 9). *M* denotes the removal of masking (Sec. 3.4), *STC* the removal of spatio-temporal contexts (Sec. 3.2), and *PCC* the removal of pose consistency constraints (Sec. 3.3).

4.6.2 Spatio-Temporal Contexts

The introduction of our proposed spatio-temporal contexts (STC), as described in Section 3.2, boosts performance on all cameras, from 0.211 to 0.202 (4.5%) on *DDAD* and 0.327 to 0.299 (9.1%) on *nuScenes*, by leveraging different levels of overlapping between views. This improvement becomes more apparent when considering our *shared median-scaling* evaluation protocol: 0.241 to 0.208 (16.1%) on *DDAD* and 0.428 to 0.355 (20.6%) on *nuScenes*. This is evidence that STC produces more consistent pointclouds across multiple cameras, as evidenced in Figure 5 and revealed by our proposed metric. Furthermore, the known extrinsics between cameras enables the generation of *scale-aware* models, with minimal degradation from their median-scaled counterparts: 0.207 versus 0.202 (2.2%) on *DDAD* and 0.311 vs 0.299 (4.0% on *nuScenes*). In this setting, we also evaluated the impact of STC relative to using only spatial and temporal contexts independently. As expected, there is a noticeable degrada-

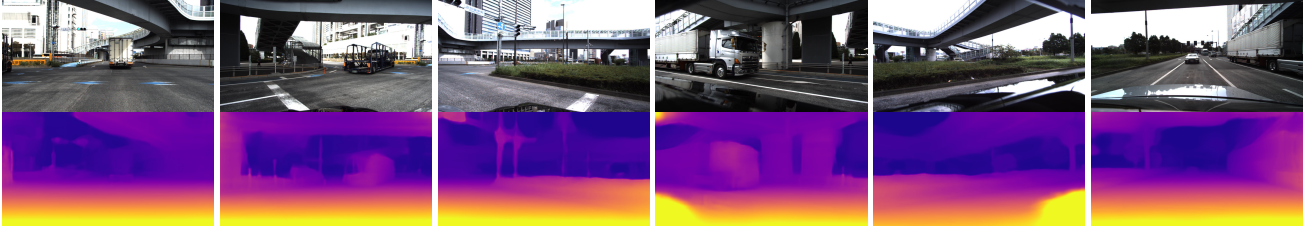


Figure 6: Self-Supervised depth estimation results using FSM on the *DDAD* dataset.

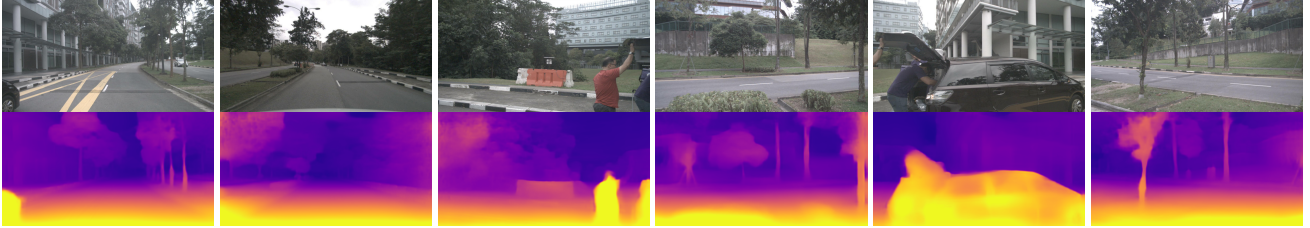


Figure 7: Self-Supervised depth estimation results using FSM on the *nuScenes* dataset.

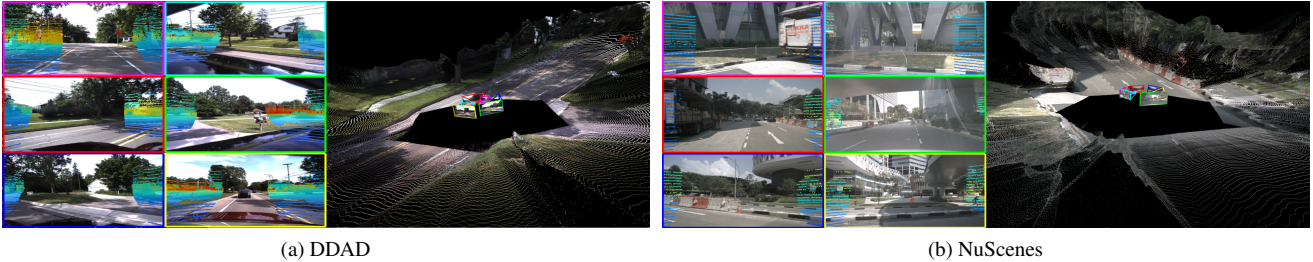


Figure 8: **Predicted pointclouds using FSM on the *DDAD* and *nuScenes* datasets.** For each dataset, the same network is used in all six images, predicted depth maps are lifted to 3D using camera intrinsics and extrinsics, and then combined *without any post-processing*. As a way to visualize camera overlapping, we also show projected LiDAR points from adjacent views overlaid on each RGB image (this information is not used at training or test time).

tion in performance when spatio-temporal contexts are not considered: 0.206 to 0.218 (5.4%) on *DDAD* and 0.311 to 0.391 (25.8%) on *nuScenes*. We hypothesize that degradation on *nuScenes* is substantially higher due to an overall smaller overlapping between cameras (Figure 8), which will benefit more from STC as a way to improve cross-camera photometric losses for self-supervised training (Figure 3).

4.6.3 Pose Consistency Constraints

Finally, we include the pose consistency constraints (PCC) described in Section 3.3, as a way to enforce the learning of a similar rigid motion for all cameras. These additional constraints further boost performance, from 0.207 to 0.201 (2.9%) on *DDAD* and 0.311 to 0.297 (4.5%) on *nuScenes*. These improvements are more prominent on the side cameras, since per-frame pose estimation is harder in these cases due to larger relative motion and smaller overlap. Interestingly, the combination of all our contributions (masking, spatio-temporal contexts and pose consistency constraints) lead to **scale-aware results that surpass**

median-scaled results. This is evidence that FSM is capable of generating state-of-the-art metrically accurate models that are useful for downstream tasks in real applications.

5. Conclusion

Using cameras for 3D perception to complement or replace LiDAR scanners is an exciting new frontier for robotics. We have extended self-supervised learning of depth and ego-motion from monocular and stereo settings to the general multi-camera setting, predicting *scale-aware* and dense point clouds around the ego-vehicle. We also introduced a series of key techniques that boost performance in this new setting by leveraging known extrinsics between cameras: *spatio-temporal contexts*, *pose consistency constraints*, and studied the effects of *non-overlapping* and *self-occlusion* photometric masking. In extensive experiments we demonstrated the capabilities of our methods and how they advance the state of the art. As future work, we plan to relax the assumption of known intrinsics and extrinsics, and estimate these parameters jointly with depth and ego-motion to enable vehicle self-calibration.

A. Network Architectures

For our experiments we use a ResNet18-based depth and pose architecture similar to [12]. For more details please refer to Table 4. Note that our FSM constraints do not require any particular depth and pose network architectures.

B. Datasets

B.1. DDAD

The Dense Depth for Automated Driving (DDAD) [15] is an urban driving dataset captured with six synchronized cameras and depth ranges of up to 250 meters. It has a total of 12,650 training samples, from which we consider all six cameras for a total of 63,250 images and ground-truth depth maps (not used in this work). The validation set contains 3,950 samples (15,800 images) and ground-truth depth maps, used only for evaluation. Following the procedure outlined in [15], input images were downsampled to a 640×384 resolution, and for evaluation we considered distances up to 200m without any cropping.

B.2. nuScenes

The nuScenes [5] dataset is an urban driving dataset that contains images from a synchronized six-camera array, comprised of 1000 scenes with a total of 1.4M images. The dataset contains 2D and 3D annotations, and is primarily used as a detection dataset. It is annotated at a 2Hz framerate, however images are captured at 30Hz, and we use the larger dataset for training. The raw images are 1600×900 , which are downsampled to 768×448 , and evaluated at distances up to 80m without any cropping. Though the data is diverse, it is also very challenging for self-supervised monocular depth estimation, containing many scenes in very low illumination, with rain droplets occluding the lens, and where the road is not visible from the side cameras (see Figure 10).

B.3. KITTI

For our stereo KITTI experiments we train and evaluate on the standard *Eigen* split [55], which is comprised of 23,488 training, 888 validation and 697 testing images. Corresponding projected depth maps for ground truth evaluation are obtained from raw LiDAR scans. Images were downsampled to 640×192 , and evaluated at distances up to 80m with the *garg* crop [55].

C. COLMAP

COLMAP [41] is a leading SfM technique used for large-scale 3D reconstruction. It takes a collection of images and produces a 3D pointcloud, from which dense depth maps can be obtained by projecting this reconstructed pointcloud onto each image plane. We use COLMAP as a “self-

	Layer Description	K	S	Out. Dim.
ResidualBlock (K, S)				
#A	Conv2d → BN → ReLU	K	1	
#B	Conv2d → BN → ReLU	K	S	
UpsampleBlock (#skip)				
#C	Conv2d → BN → ReLU → Upsample	3	1	
#D	Conv2d ($\#C \oplus \#skip$) → BN → ReLU	3	1	
#0	Input RGB image	-	-	$3 \times H \times W$
Encoder				
#1	Conv2d → BN → ReLU	7	1	$64 \times H \times W$
#2	Max. Pooling	3	2	$64 \times H/2 \times W/2$
#3	ResidualBlock (x2)	3	2	$64 \times H/4 \times W/4$
#4	ResidualBlock (x2)	3	2	$128 \times H/8 \times W/8$
#5	ResidualBlock (x2)	3	2	$256 \times H/16 \times W/16$
#6	ResidualBlock (x2)	3	2	$512 \times H/32 \times W/32$
Depth Decoder				
#7	UpsampleBlock (#5)	3	1	$256 \times H/16 \times W/16$
#8	UpsampleBlock (#4)	3	1	$128 \times H/8 \times W/8$
#9	UpsampleBlock (#3)	3	1	$64 \times H/4 \times W/4$
#10	UpsampleBlock (#2)	3	1	$32 \times H/2 \times W/2$
#11	UpsampleBlock (#1)	3	1	$32 \times H \times W$
#12	Conv2d → Sigmoid	3	1	$1 \times H \times W$

(a) Depth Network [13].

	Layer Description	K	S	Out. Dim.
#0	Input 2 RGB images	-	-	$6 \times H \times W$
#1	Conv2d → GN → ReLU	3	2	$16 \times H/2 \times W/2$
#2	Conv2d → GN → ReLU	3	2	$32 \times H/4 \times W/4$
#3	Conv2d → GN → ReLU	3	2	$64 \times H/8 \times W/8$
#4	Conv2d → GN → ReLU	3	2	$128 \times H/16 \times W/16$
#5	Conv2d → GN → ReLU	3	2	$256 \times H/32 \times W/32$
#6	Conv2d → GN → ReLU	3	2	$256 \times H/64 \times W/64$
#7	Conv2d → GN → ReLU	3	2	$256 \times H/128 \times W/128$
#8	Conv2d	1	1	$6 \times H/128 \times W/128$
#9	Global Pooling	-	-	6

(b) Pose Network [54].

Table 4: **Neural network architectures used in our proposed FSM framework.** The predicted depth maps are $1 \times H \times W$ tensors, and the predicted poses are 6-dimensional vectors representing translation (x, y, z) and Euler rotation angles (pitch, yaw, roll). *BN* stands for Batch Normalization [20], *GN* for Group Normalization [50], *Upsample* doubles spatial dimensions using bilinear interpolation, and *ReLU* denote Rectified Linear Units. The symbol \oplus indicates feature concatenation.

supervised” baseline to our method, generating pseudo-ground truth projected depth maps to train a supervised depth estimator. We used the following procedure to generate pseudo-ground truth COLMAP depth maps on the *DDAD* dataset: first, original 1936×1216 images are downsampled by 50% to 968×608 to more closely match the resolution of self-supervised learning, and to make time-intensive dataset generation more manageable. Then, for each scene we consider the set of images from all six cameras and all timesteps and generate a COLMAP pointcloud (using the default parameters, which we have found to produce best overall results on average between diverse scene types). Finally, this 3D structure is reprojected as depth maps onto each image. For some scenes, COLMAP failed to reconstruct a consistent pointcloud, leading to depth map generation only for a subset of images. Note that this proce-

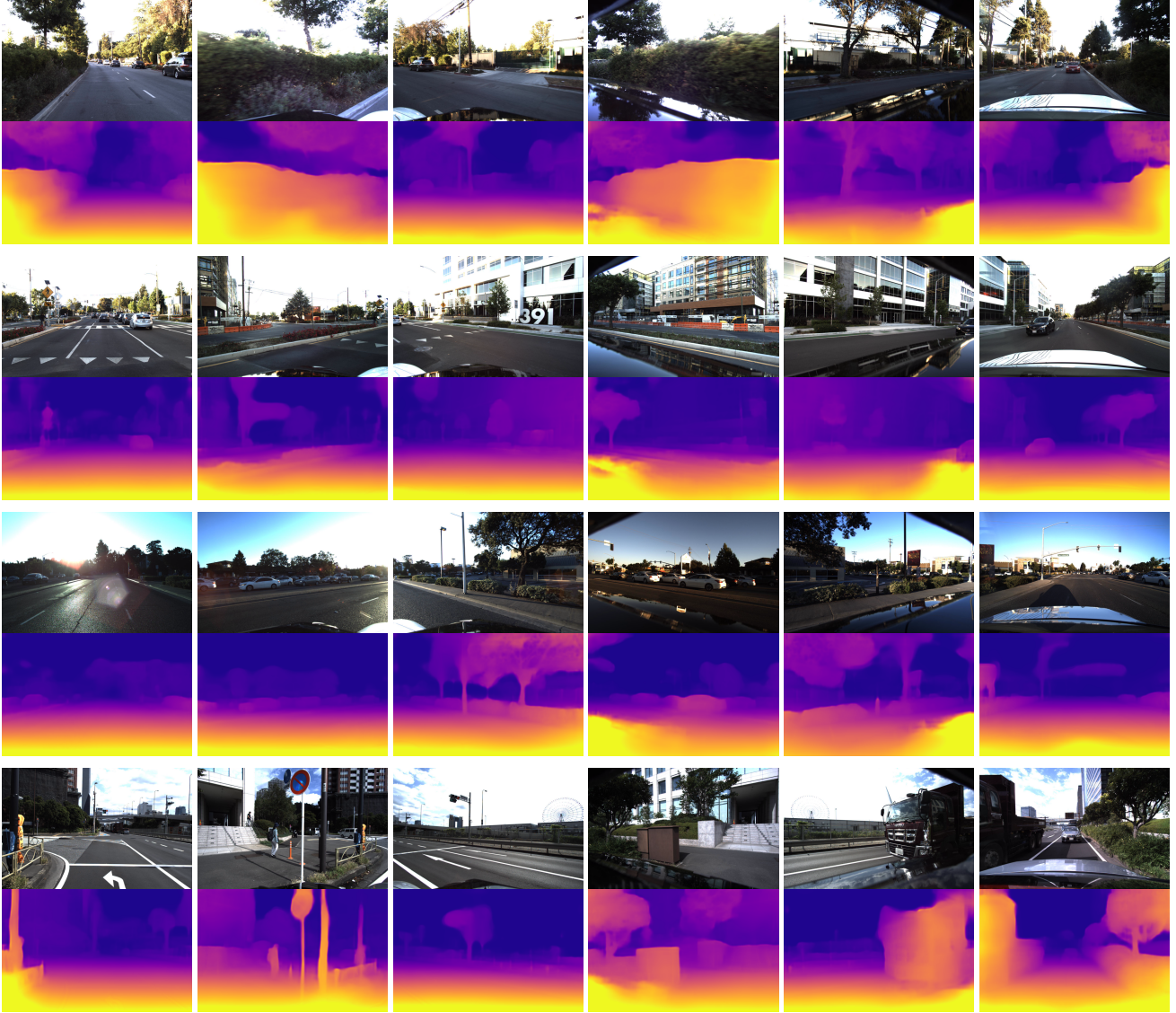


Figure 9: **Self-Supervised depth estimation FSM results** on the *DDAD* dataset. Unlike *nuScenes*, *DDAD* scenes were curated with the intent of depth estimation training, containing higher quality images with larger overlap between cameras (compare with *nuScenes* images in Figure 10). This higher data quality leads to the difference in metrics reported in the paper on these two datasets.

procedure is very time-consuming – each *DDAD* scene can take 3 – 5 GPU-hours for 3D reconstruction (thus 600 – 1000 GPU-hours for the entire dataset). In comparison, our approach to self-supervision trains the network to convergence over the entire dataset in a few hours. Using this procedure, we were able to generate pseudo-ground truth depth for approximately 80% of the *DDAD* dataset. For the COLMAP-supervised training, we used the same depth network architecture shown in Table 4a and no pose network, since there are no temporal contexts.

D. Training Details

Our models were implemented using PyTorch [37] and trained across eight V100 GPUs¹. To highlight the flexibility of our proposed framework, all experiments used the same training hyper-parameters: Adam optimizer [28], with $\beta_1 = 0.9$ and $\beta_2 = 0.999$; batch size of 4 per GPU for single camera and 6 per GPU for multi-camera (all images from each sample in the same batch); learning rate of $2 \cdot 10^{-4}$ for 20 epochs; the previous $t - 1$ and subsequent

¹Training and inference code, as well as pre-trained models, will be made available upon publication.

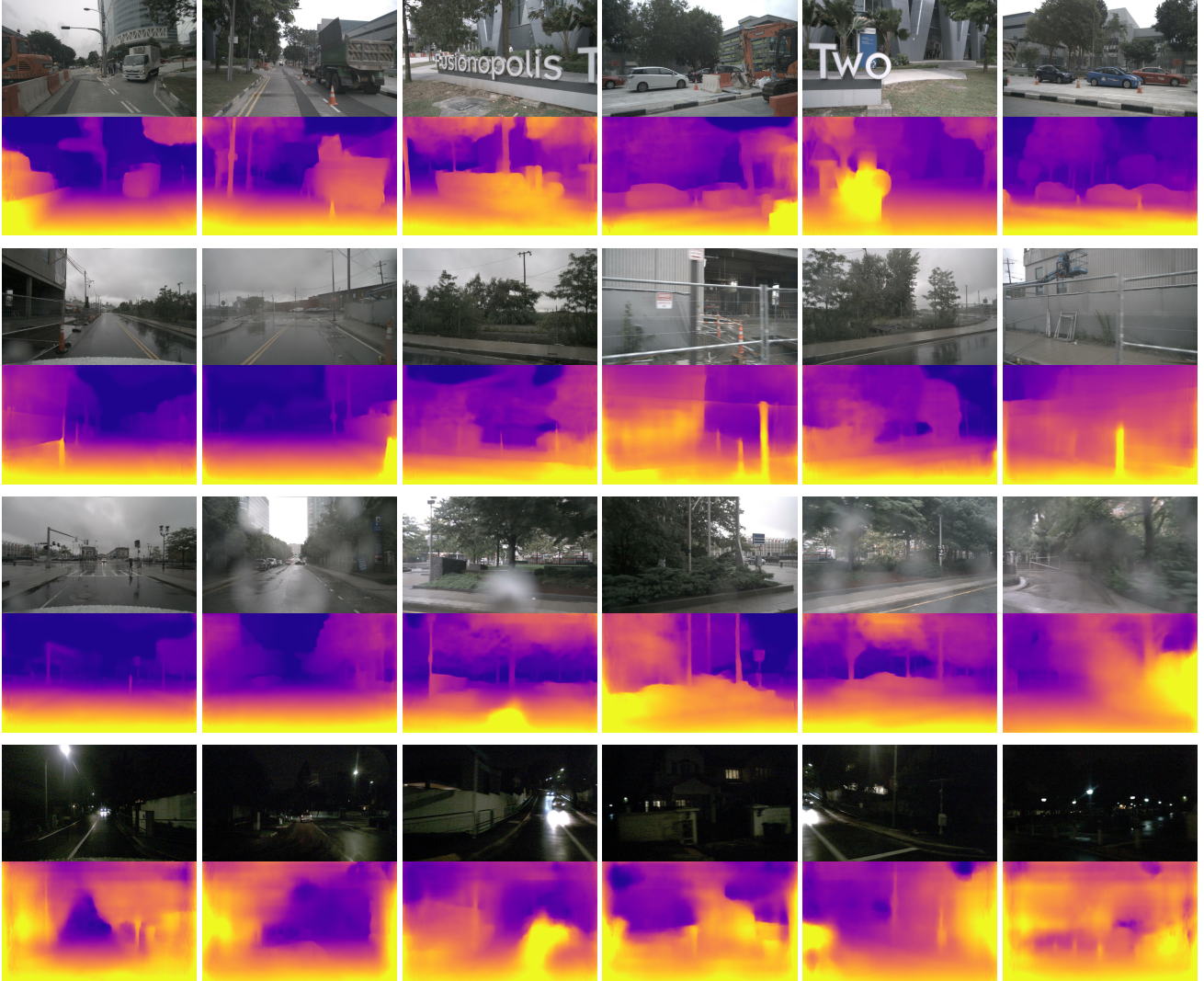


Figure 10: **Self-Supervised depth estimation FSM results** on the *nuScenes* dataset. The lower resolution and smaller overlap between cameras, combined with diverse weather conditions, time of day and observed structures (especially on side-facing cameras), make *nuScenes* a particularly challenging dataset for self-supervised multi-camera depth estimation.

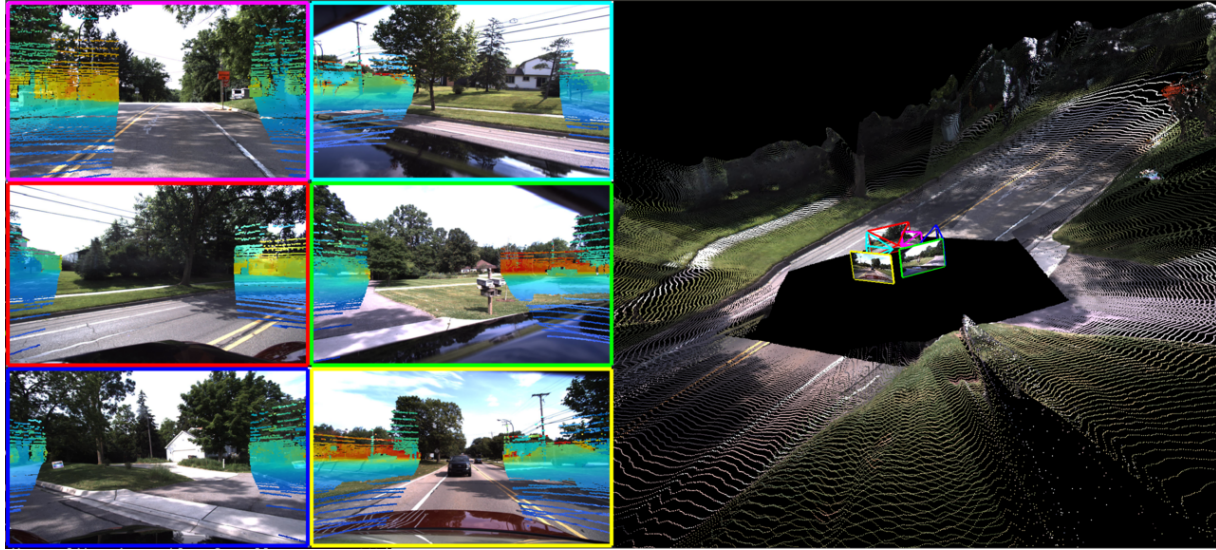
$t + 1$ images are used as temporal context; color jittering and horizontal flipping as data augmentation; SSIM weight of $\alpha = 0.85$; and depth smoothness weight of $\lambda_d = 0.001$. We also used coefficients $\lambda_s = 0.1$ and $\lambda_t = 1.0$ to weight spatial and temporal losses respectively.

E. Multi-Camera Qualitative Results

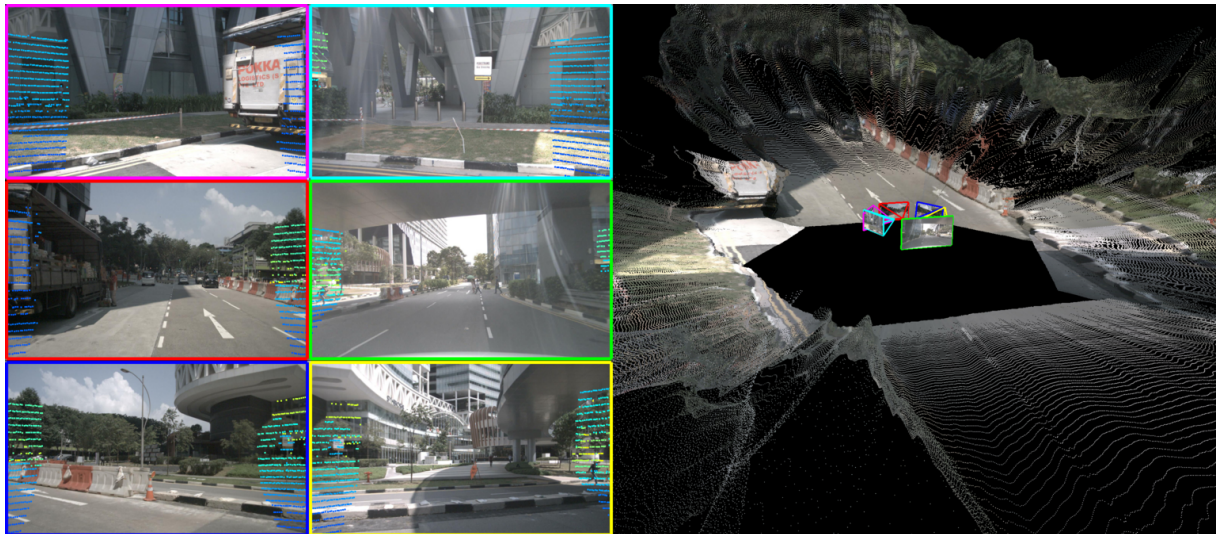
We show qualitative results for randomly-selected images from the *DDAD* dataset in Figure 9, and *nuScenes* results in Figure 10. The difference in data quality between these two datasets (image resolution, camera field-of-view overlap) is reflected in the quantitative results reported in the main paper. Even so, our proposed FSM constraints significantly boost performance in these two challenging

settings to achieve a new state of the art in self-supervised monocular depth estimation, without any changes to the underlying framework.

Similarly, in Figure 11 we show examples of reconstructed 360° pointclouds for each dataset, obtained by lifting 2D color information to 3D using predicted depth and camera calibration (intrinsics and extrinsics). We also show how much overlap there is between cameras by overlaying projected LiDAR points from adjacent views, where we can see that *DDAD* has significantly more overlap than *nuScenes*. Regardless, FSM is capable of leveraging different levels of overlap between cameras to generate consistent, scale aware pointclouds without any post-processing. A video showing examples of reconstructed sequences using FSM is also provided as supplementary material.



(a) DDAD



(b) nuScenes

Figure 11: **Predicted 360° scale-aware FSM pointclouds** on different multi-camera datasets. Each image is processed by the same network, and the predicted depth maps are lifted to 3D using camera intrinsics and extrinsics. On the left, LiDAR points from adjacent cameras are overlaid to show how much overlap there is between views.

Acknowledgments IV and GS were supported in part by AFOSR Center of Excellence Award FA9550-18-1-0166.

References

- [1] Benjamin Attal, Selena Ling, Aaron Gokaslan, Christian Richardt, and James Tompkin. Matryodshka: Real-time 6dof video view synthesis using multi-sphere images. In *European Conference on Computer Vision*, pages 441–459. Springer, 2020. 2
- [2] Tobias Bertel, Mingze Yuan, Reuben Lindroos, and Christian Richardt. Omniphotos: casual 360° vr photography. *ACM Transactions on Graphics (TOG)*, 39(6):1–12, 2020. 2
- [3] Jia-Wang Bian, Zhichao Li, Naiyan Wang, Huangying Zhan, Chunhua Shen, Ming-Ming Cheng, and Ian Reid. Unsupervised scale-consistent depth and ego-motion learning from monocular video. In *Thirty-third Conference on Neural Information Processing Systems (NeurIPS)*, 2019. 6
- [4] Myron Z Brown, Darius Burschka, and Gregory D Hager. Advances in computational stereo. *IEEE transactions on pattern analysis and machine intelligence*, 25(8):993–1008, 2003. 2
- [5] Holger Caesar, Varun Bankiti, Alex H Lang, Sourabh Vora, Venice Erin Liong, Qiang Xu, Anush Krishnan, Yu Pan, Giancarlo Baldan, and Oscar Beijbom. nuscenes: A multi-modal dataset for autonomous driving. In *Proceedings of*

- the *IEEE/CVF conference on computer vision and pattern recognition*, pages 11621–11631, 2020. 1, 2, 3, 5, 9
- [6] Hong-Xiang Chen, Kunhong Li, Zhiheng Fu, Mengyi Liu, Zonghao Chen, and Yulan Guo. Distortion-aware monocular depth estimation for omnidirectional images. *IEEE Signal Processing Letters*, 2021. 2
- [7] David Eigen and Rob Fergus. Predicting depth, surface normals and semantic labels with a common multi-scale convolutional architecture. In *Proceedings of the IEEE international conference on computer vision*, pages 2650–2658, 2015. 2
- [8] David Eigen, Christian Puhrsch, and Rob Fergus. Depth map prediction from a single image using a multi-scale deep network. *arXiv preprint arXiv:1406.2283*, 2014. 2
- [9] Ravi Garg, Vijay Kumar Bg, Gustavo Carneiro, and Ian Reid. Unsupervised cnn for single view depth estimation: Geometry to the rescue. In *European conference on computer vision*, pages 740–756. Springer, 2016. 2
- [10] Andreas Geiger, Philip Lenz, and Raquel Urtasun. Are we ready for autonomous driving? the kitti vision benchmark suite. In *Computer Vision and Pattern Recognition (CVPR), 2012 IEEE Conference on*, pages 3354–3361. IEEE, 2012. 2, 3, 5
- [11] Clément Godard, Oisín Mac Aodha, and Gabriel J Brostow. Unsupervised monocular depth estimation with left-right consistency. In *Proceedings of the IEEE Conference on Computer Vision and Pattern Recognition*, pages 270–279, 2017. 2, 3, 6
- [12] Clément Godard, Oisín Mac Aodha, Michael Firman, and Gabriel J Brostow. Digging into self-supervised monocular depth estimation. In *Proceedings of the IEEE international conference on computer vision*, pages 3828–3838, 2019. 1, 2, 3, 4, 5, 6, 7, 9
- [13] Clément Godard, Oisín Mac Aodha, Michael Firman, and Gabriel J. Brostow. Digging into self-supervised monocular depth prediction. In *ICCV*, 2019. 9
- [14] Ariel Gordon, Hanhan Li, Rico Jonschkowski, and Anelia Angelova. Depth from videos in the wild: Unsupervised monocular depth learning from unknown cameras. In *Proceedings of the IEEE/CVF International Conference on Computer Vision*, pages 8977–8986, 2019. 1, 2, 4, 5, 7
- [15] Vitor Guizilini, Rares Ambrus, Sudeep Pillai, Allan Rantos, and Adrien Gaidon. 3d packing for self-supervised monocular depth estimation. In *IEEE Conference on Computer Vision and Pattern Recognition (CVPR)*, 2020. 1, 2, 3, 5, 6, 7, 9
- [16] Vitor Guizilini, Rares Ambrus, Sudeep Pillai, Allan Rantos, and Adrien Gaidon. 3d packing for self-supervised monocular depth estimation. In *Proceedings of the IEEE/CVF Conference on Computer Vision and Pattern Recognition*, pages 2485–2494, 2020. 2
- [17] Richard Hartley and Andrew Zisserman. *Multiple view geometry in computer vision*. Cambridge university press, 2003. 3
- [18] Po-Han Huang, Kevin Matzen, Johannes Kopf, Narendra Ahuja, and Jia-Bin Huang. Deepmvs: Learning multi-view stereopsis. In *Proceedings of the IEEE Conference on Computer Vision and Pattern Recognition*, pages 2821–2830, 2018. 2
- [19] Sunghoon Im, Hae-Gon Jeon, Stephen Lin, and In So Kweon. Dpsnet: End-to-end deep plane sweep stereo. *arXiv preprint arXiv:1905.00538*, 2019. 2
- [20] Sergey Ioffe and Christian Szegedy. Batch normalization: Accelerating deep network training by reducing internal covariate shift. *arXiv preprint arXiv:1502.03167*, 2015. 9
- [21] Max Jaderberg, Karen Simonyan, Andrew Zisserman, and Koray Kavukcuoglu. Spatial transformer networks. *arXiv preprint arXiv:1506.02025*, 2015. 2
- [22] Abhishek Kar, Christian Häne, and Jitendra Malik. Learning a multi-view stereo machine. *arXiv preprint arXiv:1708.05375*, 2017. 2
- [23] Antonios Karakottas, Nikolaos Zioulis, Stamatis Samaras, Dimitrios Ataloglou, Vasileios Gkitsas, Dimitrios Zarpalas, and Petros Daras. 360° surface regression with a hypersphere loss. In *2019 International Conference on 3D Vision (3DV)*, pages 258–268. IEEE, 2019. 2
- [24] Alex Kendall and Roberto Cipolla. Geometric loss functions for camera pose regression with deep learning. In *Proceedings of the IEEE Conference on Computer Vision and Pattern Recognition*, pages 5974–5983, 2017. 4
- [25] Alex Kendall, Matthew Grimes, and Roberto Cipolla. Posenet: A convolutional network for real-time 6-dof camera relocalization. In *Proceedings of the IEEE international conference on computer vision*, pages 2938–2946, 2015. 4
- [26] Alex Kendall, Hayk Martirosyan, Saumitro Dasgupta, Peter Henry, Ryan Kennedy, Abraham Bachrach, and Adam Bry. End-to-end learning of geometry and context for deep stereo regression. In *Proceedings of the IEEE International Conference on Computer Vision*, pages 66–75, 2017. 2
- [27] Tejas Khot, Shubham Agrawal, Shubham Tulsiani, Christoph Mertz, Simon Lucey, and Martial Hebert. Learning unsupervised multi-view stereopsis via robust photometric consistency. *arXiv preprint arXiv:1905.02706*, 2019. 2
- [28] Diederik P Kingma and Jimmy Ba. Adam: A method for stochastic optimization. *arXiv preprint arXiv:1412.6980*, 2014. 10
- [29] Marvin Klingner, Jan-Aike Termöhlen, Jonas Mikolajczyk, and Tim Fingscheidt. Self-supervised monocular depth estimation: Solving the dynamic object problem by semantic guidance. In *European Conference on Computer Vision*, pages 582–600. Springer, 2020. 2
- [30] Maria Klodt and Andrea Vedaldi. Supervising the new with the old: learning sfm from sfm. In *Proceedings of the European Conference on Computer Vision (ECCV)*, pages 698–713, 2018. 6
- [31] Yevhen Kuznetsov, Jorg Stuckler, and Bastian Leibe. Semi-supervised deep learning for monocular depth map prediction. In *Proceedings of the IEEE conference on computer vision and pattern recognition*, pages 6647–6655, 2017. 2
- [32] Ruihao Li, Sen Wang, Zhiqiang Long, and Dongbing Gu. Undeepvo: Monocular visual odometry through unsupervised deep learning. In *2018 IEEE international conference on robotics and automation (ICRA)*, pages 7286–7291. IEEE, 2018. 6

- [33] Zhengqi Li and Noah Snavely. Megadepth: Learning single-view depth prediction from internet photos. In *Proceedings of the IEEE Conference on Computer Vision and Pattern Recognition*, pages 2041–2050, 2018. 6
- [34] Keyang Luo, Tao Guan, Lili Ju, Yuesong Wang, Zhuo Chen, and Yawei Luo. Attention-aware multi-view stereo. In *Proceedings of the IEEE/CVF Conference on Computer Vision and Pattern Recognition*, pages 1590–1599, 2020. 2
- [35] Reza Mahjourian, Martin Wicke, and Anelia Angelova. Unsupervised learning of depth and ego-motion from monocular video using 3d geometric constraints. In *Proceedings of the IEEE Conference on Computer Vision and Pattern Recognition*, pages 5667–5675, 2018. 5
- [36] Pushmeet Kohli, Nathan Silberman, Derek Hoiem, and Rob Fergus. Indoor segmentation and support inference from rgb-d images. In *ECCV*, 2012. 2
- [37] Adam Paszke, Sam Gross, Soumith Chintala, Gregory Chanan, Edward Yang, Zachary DeVito, Zeming Lin, Alban Desmaison, Luca Antiga, and Adam Lerer. Automatic differentiation in pytorch. In *NIPS-W*, 2017. 10
- [38] Sudeep Pillai, Rares Ambrus, and Adrien Gaidon. Superdepth: Self-supervised, super-resolved monocular depth estimation. In *IEEE International Conference on Robotics and Automation (ICRA)*, May 2019. 5, 6
- [39] Ashutosh Saxena, Jamie Schulte, Andrew Y Ng, et al. Depth estimation using monocular and stereo cues. In *IJCAI*, volume 7, pages 2197–2203, 2007. 2
- [40] Ashutosh Saxena, Min Sun, and Andrew Y Ng. Make3d: Learning 3d scene structure from a single still image. *IEEE transactions on pattern analysis and machine intelligence*, 31(5):824–840, 2008. 2
- [41] Johannes L Schonberger and Jan-Michael Frahm. Structure-from-motion revisited. In *Proceedings of the IEEE conference on computer vision and pattern recognition*, pages 4104–4113, 2016. 6, 9
- [42] Alisha Sharma and Jonathan Ventura. Unsupervised learning of depth and ego-motion from cylindrical panoramic video. In *2019 IEEE International Conference on Artificial Intelligence and Virtual Reality (AIVR)*, pages 58–587. IEEE, 2019. 2
- [43] Igor Vasiljevic, Vitor Guizilini, Rares Ambrus, Sudeep Pillai, Wolfram Burgard, Greg Shakhnarovich, and Adrien Gaidon. Neural ray surfaces for self-supervised learning of depth and ego-motion. In *3DV*, 2020. 2
- [44] Fu-En Wang, Yu-Hsuan Yeh, Min Sun, Wei-Chen Chiu, and Yi-Hsuan Tsai. Bifuse: Monocular 360 depth estimation via bi-projection fusion. In *Proceedings of the IEEE/CVF Conference on Computer Vision and Pattern Recognition*, pages 462–471, 2020. 2
- [45] Ning-Hsu Wang, Bolivar Solarte, Yi-Hsuan Tsai, Wei-Chen Chiu, and Min Sun. 360sd-net: 360° stereo depth estimation with learnable cost volume. In *2020 IEEE International Conference on Robotics and Automation (ICRA)*, pages 582–588. IEEE, 2020. 2
- [46] Yan Wang, Wei-Lun Chao, Divyansh Garg, Bharath Hariharan, Mark Campbell, and Kilian Q Weinberger. Pseudo-lidar from visual depth estimation: Bridging the gap in 3d object detection for autonomous driving. In *Proceedings of the IEEE Conference on Computer Vision and Pattern Recognition*, pages 8445–8453, 2019. 2
- [47] Yang Wang, Peng Wang, Zhenheng Yang, Chenxu Luo, Yi Yang, and Wei Xu. Unos: Unified unsupervised optical-flow and stereo-depth estimation by watching videos. In *Proceedings of the IEEE/CVF Conference on Computer Vision and Pattern Recognition*, pages 8071–8081, 2019. 3
- [48] Zhou Wang, Alan C Bovik, Hamid R Sheikh, and Eero P Simoncelli. Image quality assessment: from error visibility to structural similarity. *IEEE transactions on image processing*, 13(4):600–612, 2004. 2
- [49] Changhee Won, Jongbin Ryu, and Jongwoo Lim. Omnimvs: End-to-end learning for omnidirectional stereo matching. In *Proceedings of the IEEE/CVF International Conference on Computer Vision*, pages 8987–8996, 2019. 2
- [50] Yuxin Wu and Kaiming He. Group normalization. In *Computer Vision - ECCV 2018 - 15th European Conference, Munich, Germany, September 8-14, 2018, Proceedings, Part XIII*, pages 3–19, 2018. 9
- [51] Youze Xue, Jiansheng Chen, Weitao Wan, Yiqing Huang, Cheng Yu, Tianpeng Li, and Jiayu Bao. Mvsrfl: Learning multi-view stereo with conditional random fields. In *Proceedings of the IEEE/CVF International Conference on Computer Vision*, pages 4312–4321, 2019. 2
- [52] Jure Zbontar, Yann LeCun, et al. Stereo matching by training a convolutional neural network to compare image patches. *J. Mach. Learn. Res.*, 17(1):2287–2318, 2016. 2
- [53] Huangying Zhan, Ravi Garg, Chamara Saroj Weerasekera, Kejie Li, Harsh Agarwal, and Ian Reid. Unsupervised learning of monocular depth estimation and visual odometry with deep feature reconstruction. In *Proceedings of the IEEE Conference on Computer Vision and Pattern Recognition*, pages 340–349, 2018. 2
- [54] Lipu Zhou, Jiamin Ye, Montiel Abello, Shengze Wang, and Michael Kaess. Unsupervised learning of monocular depth estimation with bundle adjustment, super-resolution and clip loss. *arXiv preprint arXiv:1812.03368*, 2018. 9
- [55] Tinghui Zhou, Matthew Brown, Noah Snavely, and David G Lowe. Unsupervised learning of depth and ego-motion from video. In *Proceedings of the IEEE Conference on Computer Vision and Pattern Recognition*, pages 1851–1858, 2017. 1, 2, 5, 9